

dards were obtained from common commercial sources and dissolved in Milli-Q (Millipore) water, 0.1 mol L<sup>-1</sup> HCl, or 0.1 mol L<sup>-1</sup> NaOH to furnish 10 mmol L<sup>-1</sup> or 100 mmol L<sup>-1</sup> stock solutions. Distilled water purified by use of a Milli-Q water system was used for all the preparations. Working standard mixtures were prepared by diluting stock solutions with Milli-Q water immediately before injection of samples for CE-MS analysis. The chemicals used were analytical or reagent grades.

#### Animal model to observe growth of human-derived cancer in vivo

Care and use of laboratory animals were in accordance with the Experimental Animal Committee of Keio University School of Medicine which followed the Guidelines for the Proper Conduct of Animal Experiments by the Science Council of Japan. We herein applied an experimental model using superimmunodeficient NOD/SCID/IL-2R $\gamma$ <sup>null</sup> (NOG) mice [18] which lack T-cells, B-cells, and NK cells, enabling xenograft transplantation of the human-derived colon cancer cell line HCT116 transfected with *venus*, a GFP-mutant gene (HCT116/*venus*) was injected intrasplenically as described elsewhere [17, 19]. To our knowledge, the system using NOG mice serves as a reliable experimental model in which human-derived cancer cell lines transplanted in vivo generate metastases forming solid tumors in organs including the liver in vivo with greater reproducibility than the conventional model using NOD mice which lack T-cells and B-cells but not NK cells [17]. In the intrasplenic implantation model using HCT116/*venus*, micrometastases of the cancer occurred mostly in periportal regions of the liver within one week, extending their size over the following three weeks [19]. In this study, male mice at 11–13 weeks were fed with Laboratory chow and allowed free access to water. They were anesthetized by use of pentobarbital sodium, and their abdominal walls were cut to exteriorize the portion of the liver lobules for snap-frozen procedures using liquid nitrogen as described elsewhere [20, 21]. The livers of the xenograft-transplanted NOG mice used for the analyses were collected under fed conditions two weeks after the xenograft transplantation, unless otherwise mentioned.

#### Tissue preparation

A schematic diagram of a standard experimental design typical of tissue section application can be seen in the Electronic Supplementary Material (Fig. S1). The liver tissues snap-frozen in liquid nitrogen were dissected to prepare cryosections with 5- $\mu$ m thickness by use of a cryostat (CM 1900; Leica Microsystems, Wetzlar, Germany). The sections were thaw-mounted on indium-tin oxide (ITO) slides (8–12 ohm/sq; Sigma, Chiba, Japan) and

were dried in silica gel-containing plastic tubes then sprayed with 9-aminoacridine (9-AA, 20 mg in 4 mL 70% MeOH) by use of a 0.2-mm nozzle caliber airbrush (Procon boy FWA Platinum; Mr Hobby, Tokyo, Japan) to conduct MALDI-IMS in negative ion mode. Adjacent sections were fixed with 10% buffered formalin (Nacalai Tesque, Kyoto, Japan) and stained with the Masson trichrome staining reagent kit according to the manufacturer's procedures (Muto Pure Chemicals, Tokyo, Japan). The other frozen tissues were used for metabolome analyses using CE-MS.

#### Instruments

An atmospheric pressure MALDI-QIT-TOF-MS equipped with a 355-nm Nd:YAG laser and a built-in fluorescence microscope furnished mass images with high spatial resolution of 10  $\mu$ m, as described for a prototype IMS machine [9] (Mass Microscope; Shimadzu, Kyoto, Japan). The microscope was also equipped with a 120-W metal halide light source (X-Cite 120PC-Q; Lumen Dynamics Group, Ontario, Canada) and a fluorescence mirror unit (U-MGFPHQ; Olympus, Tokyo, Japan) that enabled us to visualize *venus*-associated green fluorescence from metastatic foci in tissue slices before matrix application. This system thus enabled us to collect both fluorescence images and mass images from the same tissue slices. Before applying matrices, a fluorescence image of the analyte was acquired and followed by recording the location of the specimen on the XYZ stage. ITO slides with the sample holder were removed from the XYZ stage, and sprayed uniformly with 4 mL 9-AA solution. After application of the matrix, the sample holder was placed back on the XYZ stage, which was adjusted to exactly the same location. The mass spectra of the designated areas on a specimen photographed before matrix application were acquired in the negative-ion mode. The data collected through the microscopic system were digitally processed according to the method described later, in the section “*Determination of the apparent contents of metabolites based on data calibration by CE-MS*”. Experiments using capillary electrophoresis electrospray ionization mass spectrometry (CE-MS) were performed with a capillary electrophoresis system equipped with an air pressure pump, MSD quadrupole MS, isocratic HPLC pump, and CE-MS adapter kit (Agilent Technologies, Waldbronn, Germany) [20, 22]. All system control, data acquisition, and MSD data evaluation were performed using Agilent G2201A ChemStation software for CE-MSD.

#### Conditions for MALDI imaging and tandem MS analyses

All the MALDI imaging experiments and tandem MS experiments were carried out in negative-ion mode using a prototype mass microscope. The laser power was adjusted

to the desired intensities. MALDI mass spectra were acquired under the conditions laser frequency 800 Hz and scanning mass range from  $m/z$  260 to  $m/z$  900. Regions of the tissue samples exposed to the laser irradiation were determined by light and fluorescence microscopic observations. A raster scan on the tissue surface was performed automatically (250×250 spots per scan). Laser irradiation was repeated 160 times for the individual spots. The spatial interval of data points was 10  $\mu\text{m}$ , giving 62,500 data points in total for each section. Tandem MS analyses were performed to determine the structures of metabolites at appropriate laser energy, argon gas percentage, and collision-induced dissociation (CID) energy conditions. To identify metabolites detected in MALDI-IMS, we searched the Human Metabolome Database (<http://hmdb.ca>) and performed tandem MS analyses, comparing the tandem mass spectra with those from standard reagents using 9-AA as the matrix of choice in negative mode. The distribution of biomolecules that were identified by MS<sup>2</sup> analysis were visualized as mass images using BioMap software (<http://www.maldi-msi.org>) from Novartis (Basel, Switzerland).

#### Determination of the apparent contents of metabolites based on data calibration by CE-MS

To compare differences in contents of many different metabolites in multiple tissue slices collected from different subjects, we conducted CE-MS-based metabolome analyses of tissue lysates collected from the same snap-frozen liver samples for IMS. As reported previously [20–22], CE-MS enabled us to quantitatively determine more than 2,000 different metabolites at once in small amounts of a single liver sample. Small amounts of the frozen tissue were collected from thick section that was adjacent to the section for IMS. The CE-MS samples weighing approximately 300 mg wet weight was ground using a multi-bead shocker (model MB755U; Yasui Kikai, Osaka, Japan) with frozen metal granules, and 1 mL methanol containing internal standards (300  $\mu\text{mol L}^{-1}$  each of L-methionine sulfone and 2-morpholinoethanesulfonic acid (MES)) was added. After addition of 0.5 mL deionized water and 1 mL chloroform, the mixture was centrifuged at 15,000 rpm for 15 min at 4 °C. The upper aqueous layer of the sample was filtered through the 5-kDa cutoff filter (Millipore, Tokyo, Japan) by centrifugation to remove protein components. The filtrate was lyophilized and dissolved in 200  $\mu\text{L}$  deionized water containing reference compounds (200  $\mu\text{mol L}^{-1}$  each of 3-aminopyrrolidine and trimesate). The amounts of metabolites were normalized by liver weight of the original tissue samples. Assuming that 1 mg wet tissue was equivalent to 1  $\mu\text{L}$ , apparent contents of individual metabolites were calculated for the data calibration in imaging mass microscopy by computer-assisted data processing in the later session.

To semi-quantify apparent contents of individual metabolites mapped on the images, regions of interest (ROIs) for the cancer xenografts and the liver parenchyma were selected by careful visual inspection of fluorescence and light microscopic images. Averaged spectra from each ROI were generated and statistically analyzed by use of the laboratory-written software SIMtools (Shimadzu Imaging Mass spectrometry toolbox for MATLAB). The Mann-Whitney U-test was used to compare the ion signal intensity between the tumor and the liver parenchyma.

To calculate apparent contents of metabolites in IMS, mass signals covering  $m/z$  between 260 and 620 were collected from 250×250 spots on a tissue sample. Direct comparison of metabolite ion signals among different slices requires realistic transformation of acquired mass signals of a metabolite in absolute terms, for example tissue contents in  $\text{nmol g}^{-1}$  tissue. To that effect, apparent contents of a specific metabolite in the ROI designated as liver parenchyma ( $[C_{\text{Liver}}]_{\text{app}}$ ) or tumor ( $[C_{\text{Tumor}}]_{\text{app}}$ ) were calculated by use of Eqs. 1, 2, and 3:

$$[C_{\text{Tumor}}]_{\text{app}} = [C_{\text{Average}}] \times (I_{\text{Tumor}}/I_{\text{Average}}) \quad (1)$$

$$[C_{\text{Liver}}]_{\text{app}} = [C_{\text{Average}}] \times (I_{\text{Liver}}/I_{\text{Average}}) \quad (2)$$

$$I_{\text{Average}} = (I_{\text{Liver}} \times O_{\text{Liver}})/100 + (I_{\text{Tumor}} \times O_{\text{Tumor}})/100 \quad (3)$$

where  $[C_{\text{Average}}]$  denotes the amount of a metabolite of interest in the whole tissue section for IMS ( $\text{nmol g}^{-1}$  tissue).  $I_{\text{Tumor}}$ ,  $I_{\text{Liver}}$ , and  $I_{\text{Average}}$  are MALDI signal intensities measured in regions of tumor metastases, liver parenchyma, and the whole tissue section, respectively.  $O_{\text{Tumor}}$  and  $O_{\text{Liver}}$  are the percentage areas of tumor regions and liver parenchyma, respectively, in tumor-bearing livers. These indices were designated by the green fluorescence intensities acquired by fluorescence microscopy of the whole frozen section using Image J software (NIH, <http://rsbweb.nih.gov/ij/index.html>). Assuming that percentages of tumor-bearing regions in the tissue sections are comparable with those of the metastases in the adjacent tissue samples for the CE-MS measurements, the values of  $[C_{\text{Average}}]$  can be replaced by  $[C_{\text{CE-MS}}]$ , the amounts of the metabolites of interest in the tissue samples for CE-MS, as seen in Eqs. 1' and 2'.

$$[C_{\text{Tumor}}]_{\text{app}} = [C_{\text{CE-MS}}] \times (I_{\text{Tumor}}/I_{\text{Average}}) \quad (1')$$

$$[C_{\text{Liver}}]_{\text{app}} = [C_{\text{CE-MS}}] \times (I_{\text{Liver}}/I_{\text{Average}}) \quad (2')$$

In order to calculate the values for  $[C_{\text{Tumor}}]_{\text{app}}$  and  $[C_{\text{Liver}}]_{\text{app}}$ ,  $I_{\text{Tumor}}$ ,  $I_{\text{Liver}}$ , and  $I_{\text{Average}}$  were determined in

three different ROIs in a single tissue specimen, while the corresponding value of  $[C_{\text{CE-MS}}]$  was collected from a portion of the tissue adjacent to the samples for IMS. A set of mass-imaging data paired with CE-MS data in a single animal were repeated for four separate animals.

To construct an ion-content map, data collected by MALDI-QIT-MS were saved and digitally processed to be converted to Analyze format, a common multidimensional biomedical imaging format file. The Analyze format file was processed to construct an ion-content map, where the relationship between the apparent content of a metabolite of interest at a pixel " $i$ " ( $C_i$ ) and the MALDI signal intensity in the same pixel ( $I_{(i)}$ ) was expressed by Eq. 4:

$$C_i = [C_{\text{CE-MS}}] \times (I_{(i)} / I_{\text{Average}}) \quad (4)$$

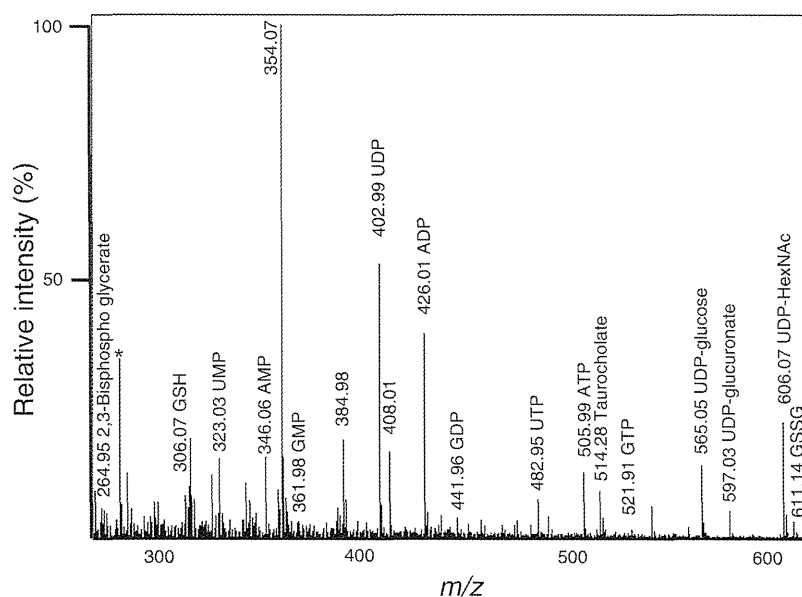
Validation of the calibrated data in IMS by analysis of high-energy adenylates in vivo

Reliability of the calibrated data seemed to depend on multiple factors including the quality of CE-MS-based metabolome analysis and that of tissue-sampling procedures in the snap-frozen processes. In accordance with our previous studies [7], we determined apparent contents of ATP, ADP, and AMP by IMS combined with CE-MS. Based on these data, apparent energy charge of individual pixels were calculated by use of Eq. 5:

Apparent energy charge ( $EC_{\text{app}}$ ) =

$$([ATP]_{\text{app}} + 1/2[ADP]_{\text{app}}) / ([ATP]_{\text{app}} + [ADP]_{\text{app}} + [AMP]_{\text{app}}) \quad (5)$$

**Fig. 1** Typical MALDI mass spectrum of the mouse liver collected from the "mass microscope" a MALDI-IT-TOF analyzer in the negative-ion mode. The signals ranging from  $m/z=260$  to 620 were collected. Mass spectra of metabolites were obtained by integrating 10,000,000 consecutive laser shots (160 shots per subspectrum and 62,500 subspectra). Peaks identified in this study are labeled; that originating from the 9-AA matrix is indicated by an asterisk



## Statistics

Differences between mean values for two groups were statistically analyzed by use of the Mann-Whitney  $U$ -test.  $P < 0.05$  was considered statistically significant.

## Results and discussion

### Detection of metabolites from normal mouse liver tissue

As shown in Fig. 1, MALDI-MS analyses in the negative-ion mode using 9-AA as the matrix revealed the presence of many signals including nucleotides on the liver tissue frozen section with minimal interference from the matrix, as reported by Edwards and Kennedy [6]. Among these peaks, 16 intense mass peaks were assigned using their exact masses to nucleotides, nucleotide-sugar conjugates, 2,3-bisphosphoglycerate (2,3-BPG), taurocholate, and both reduced and oxidized forms of glutathione. Assignment of these metabolites was verified by structural analysis of individual peaks using tandem MS. In the region adjacent to those for mass-imaging experiments in the same section, the peaks generated on the tissue surface were identified by fragmentation using MALDI-QIT-TOF MS [9]. Table 1 summarizes the results of MS and MS<sup>2</sup> analyses. Among the individual mass peaks of nucleoside-monophosphate, the ribose-phosphate structure was present (211.0 fragment ions and neutral losses of adenine, uridine, and guanine from precursor ions respectively). Among the peaks of nucleotide-sugar conjugates, fragment ions derived from the UDP structure were confirmed (403.0 fragment ions and

**Table 1** List of metabolites identified in the study, with their respective deprotonated  $m/z$  values and MS<sup>2</sup> ion species in the negative mode

No.	[M-H] <sup>-</sup> ( $m/z$ )	Fragments observed in MS <sup>2</sup>	Formula	Identified
1	264.95	246.973, 179.043, 166.955	C <sub>3</sub> H <sub>8</sub> O <sub>10</sub> P <sub>2</sub>	2,3-Bisphosphoglycerate
2	306.07	254.087, 179.050, 143.048, 158.932, 210.092, 288.858, 120.041	C <sub>10</sub> H <sub>17</sub> N <sub>3</sub> O <sub>6</sub> S	Glutathione (GSH)
3	323.02	211.006, 280.028, 138.983, 158.922	C <sub>9</sub> H <sub>13</sub> N <sub>2</sub> O <sub>9</sub> P	UMP
4	403.00	304.984, 158.907, 384.935, 322.989, 290.931, 272.920	C <sub>9</sub> H <sub>14</sub> N <sub>2</sub> O <sub>12</sub> P <sub>2</sub>	UDP
5	482.93	384.927, 272.919, 176.913, 158.905	C <sub>9</sub> H <sub>15</sub> N <sub>2</sub> O <sub>15</sub> P <sub>3</sub>	UTP
6	346.05	211.000, 150.985, 134.049, 194.051	C <sub>10</sub> H <sub>14</sub> N <sub>5</sub> O <sub>7</sub> P	AMP
7	426.02	328.044, 134.053, 407.999, 329.037, 272.950, 290.945	C <sub>10</sub> H <sub>15</sub> N <sub>5</sub> O <sub>10</sub> P <sub>2</sub>	ADP
8	505.98	408.022, 272.958, 158.922, 176.933, 392.003	C <sub>10</sub> H <sub>16</sub> N <sub>5</sub> O <sub>13</sub> P <sub>3</sub>	ATP
9	361.98	210.985, 260.838, 158.908	C <sub>10</sub> H <sub>14</sub> N <sub>5</sub> O <sub>8</sub> P	GMP
10	441.96	343.992, 150.025, 158.909	C <sub>10</sub> H <sub>15</sub> N <sub>5</sub> O <sub>11</sub> P <sub>2</sub>	GDP
11	521.91	423.940, 272.924, 176.911, 158.906, 229.979	C <sub>10</sub> H <sub>16</sub> N <sub>5</sub> O <sub>14</sub> P <sub>3</sub>	GTP
12	565.03	323.024, 306.072, 402.984, 211.000, 384.977	C <sub>15</sub> H <sub>24</sub> N <sub>2</sub> O <sub>17</sub> P <sub>2</sub>	UDP-glucose (UDP-Hexose)
13	579.02	323.027, 402.997, 254.996, 305.011, 210.994	C <sub>15</sub> H <sub>22</sub> N <sub>2</sub> O <sub>18</sub> P <sub>2</sub>	UDP-glucuronic acid
14	606.06	384.9445, 402.996, 282.045, 272.956, 323.038, 305.017, 362.008	C <sub>17</sub> H <sub>27</sub> N <sub>3</sub> O <sub>17</sub> P <sub>2</sub>	UDP-GlcNAc (UDP-HexNAc)
15	611.14	306.071, 272.086, 338.058, 254.079, 482.103, 304.058, 288.058, 593.121	C <sub>20</sub> H <sub>32</sub> N <sub>6</sub> O <sub>12</sub> S <sub>2</sub>	Glutathione, oxidized (GSSG)

neutral loss of each hexose, glucuronic acid, and *N*-acetylhexosamines). All the assigned and verified metabolites in Table 1 were compared with commercial standard compounds under appropriate MALDI and CID tandem MS conditions.

#### Intralobular distributions of metabolites in the liver

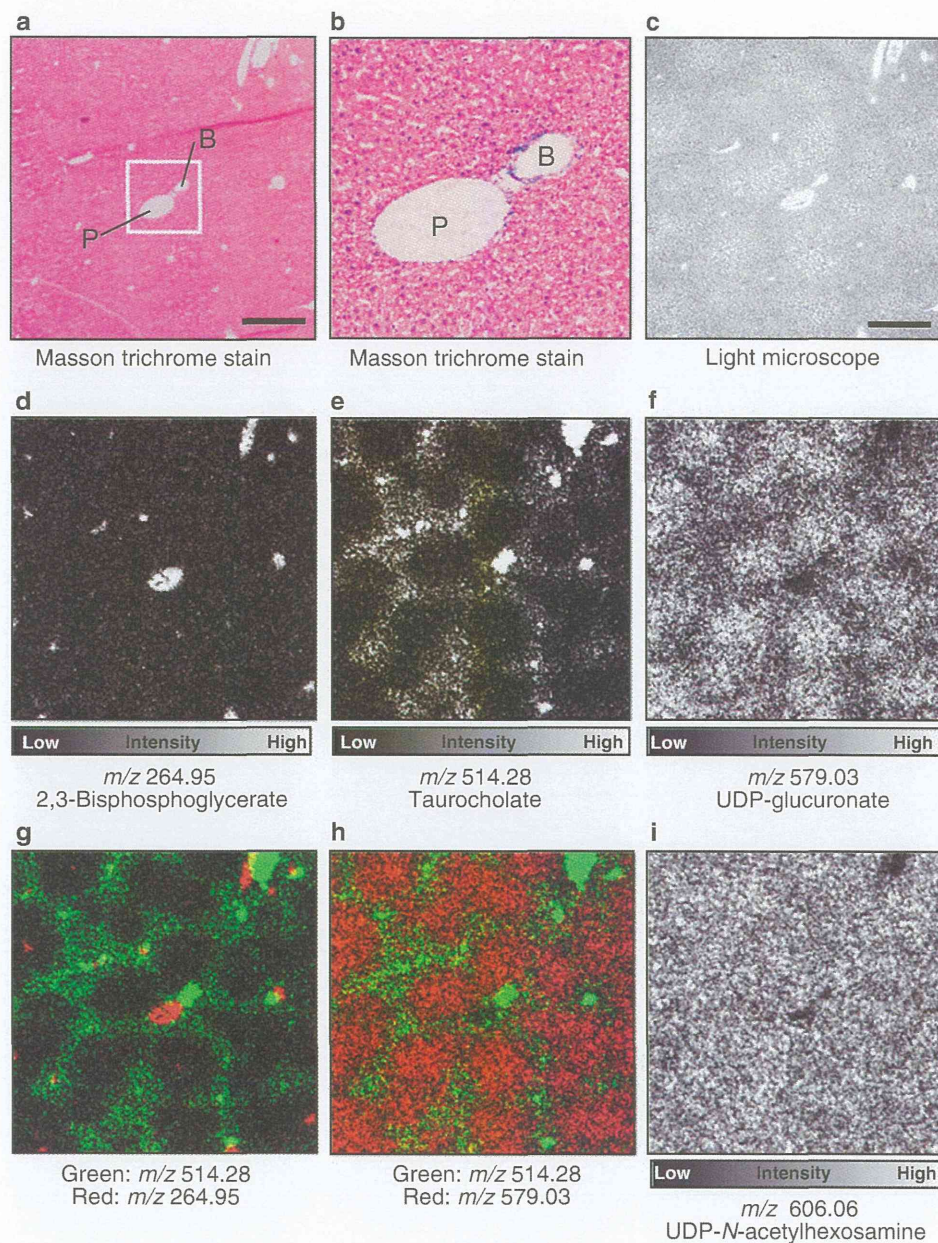
Figure 2 shows the tissue distribution of metabolites in the control fed liver of NOG mice. As seen in Figs. 2a and b, by use of Masson trichrome staining we were able to distinguish portal and central venules by judging the presence of bile ducts as a typical structure of the portal triad. Worthy of note is that the intraluminal space of the portal (P) and central venules indicated strong signals of 2,3-BPG (Fig. 2d) whereas taurocholate, the taurine-conjugated form of cholic acid, was evident in bile ducts (B) adjacent to the portal venules and periportal parenchyma, showing a typical P–P bridging pattern (Fig. 2e). On the other hand, UDP-glucuronate, a substrate for glucuronidation of xenobiotic compounds was localized mainly in pericentral regions, with a pattern distinct from that of taurocholate (Fig. 2f). Such an intralobular microanatomical relationship among periportal and pericentral regions and the microvessels was well demonstrated by superimposition of taurocholate ( $m/z$  514.28; green in Figs. 2g and h) with 2,3-BPG ( $m/z$  264.95; red in Fig. 2g) or UDP-glucuronate ( $m/z$  579.03; red in Fig. 2h), respectively. In contrast, an intralobular pattern of UDP-HexNAc was distinct, distributing homogeneously over the whole liver parenchyma (Fig. 2i). These results suggest that several different

metabolites such as 2,3-BPG, taurocholate, and UDP-glucuronate visualized by use of this method serve as reliable markers to distinguish vascular structures and periportal and pericentral regions in hepatic zonation. Such results were also consistent with previous observations as follows. First, 2,3-BPG occurs abundantly in red blood cells, being at approximately 5 mmol L<sup>-1</sup> [23]. Secondly, taurocholate is synthesized and excreted to bile canaliculi around periportal hepatocytes [24, 25], whereas UDP-glucuronate is biosynthesized predominantly in pericentral hepatocytes, which had a large capacity for xenobiotic detoxification [26, 27]. Our approach to analysis of metabolites at the microscopic level, serves as a powerful tool to investigate intralobular heterogeneity in metabolic systems in the liver.

#### Distinct properties of energy metabolism between cancer metastases and liver parenchyma

Figure 3 shows representative pictures of high-energy adenylate phosphates in liver bearing colon cancer metastases under fed conditions. As seen in Figs. 3a and b, the micrometastases were clearly identified by green fluorescence generated by *venus*-expressing HCT116 cells. Figure 3c depicts mapping of apparent energy charge that was calculated from images of AMP, ADP, and ATP (Figs. 3d, e, and f, respectively). Worthy of note was that intralobular distribution of these three adenylates appeared almost homogeneous, whereas the energy charge composed from these images had a heterogeneous pattern, being greater at the sites of cancer metastasis than in the liver

**Fig. 2** In situ mass spectrometric imaging of metabolites in the control liver of an NOG mouse. **a** An optical image of a section stained with Masson's trichrome solutions. The stained section was adjacent to that was used for IMS. *Scale bar*: 500  $\mu\text{m}$ . *B*: bile duct, *P*: portal venule. **b** The image with greater magnification of the area indicated by the white square in **a**. Collagen fibers in the portal triad were stained in blue. *B*: bile duct, *P*: portal venule. **c** Light-microscopic image of frozen liver section used in mass spectrometric imaging that was captured before matrix application. *Scale bar*: 500  $\mu\text{m}$ . **d** An ion image of 2,3-bisphosphoglycerate (2,3-BPG) at  $m/z=264.95$  and **e** taurocholate at  $m/z=514.28$ , **f** UDP-glucuronate at  $m/z=579.03$ . **g** The overlaid image of 2,3-BPG (red) and taurocholate (green). **h** UDP-glucuronate (red) and taurocholate (green). **i** UDP-HexNAc at  $m/z=606.06$ . A representative set of pictures from four separate experiments



parenchyma. So far as judged from the intensities, the apparent energy charge in the metastatic foci was approximately 0.8, while that in the parenchyma was 0.5–0.7, suggesting that the foci accelerate generation of high-energy adenylate phosphates. Of importance were semi-quantitative values of  $[\text{ATP}]_{\text{app}}$  in the tumor-bearing liver (Fig. 3f), in the range of approximately 1–2  $\mu\text{mol g}^{-1}$  liver, levels reasonably comparable with previous observations that determined absolute ATP contents under the snap-frozen procedures [20, 21]. Because intracellular levels of ATP are in the  $\text{mmol L}^{-1}$  range, current procedures for data calibration seemed to reproduce reliable intracellular concentrations of metabolites with a rapid turnover.

Glutathione and UDP-HexNAc serve as marker metabolites enriched in the cancer xenografts

Figure 4 shows representative pictures of UDP-HexNAc, reduced (GSH), and oxidized (GSSG) forms of glutathione. As seen in Figs. 4a–c, UDP-HexNAc was predominantly high in the tumor metastases. GSH and GSSG signals were also greater in the metastatic foci, but with a different pattern from that of UDP-HexNAc (Figs. 4d–f). When focusing on individual foci, UDP-HexNAc and GSH seemed to be demarcated from each other, suggesting these molecules occur in a spatially heterogeneous manner in an individual metastatic focus.

**Fig. 3** Representative pictures indicating high-energy adeny-late phosphates and apparent energy charge in the tumor-bearing livers of NOG mice.

**a** A light-microscopic photograph of intrasplenically injected HCT116 colon cancer cell xenografts. *Scale bar: 500  $\mu$ m.*

**b** A green fluorescence image of the same region shown in (a). *Scale bar: 500  $\mu$ m.*

**c** A heat map of apparent energy charge calculated from apparent contents of tumor bearing-liver.

**d–f** Heat maps of  $[AMP]_{app}$ ,  $[ADP]_{app}$ , and  $[ATP]_{app}$ , respectively. A representative set of pictures from four separate experiments

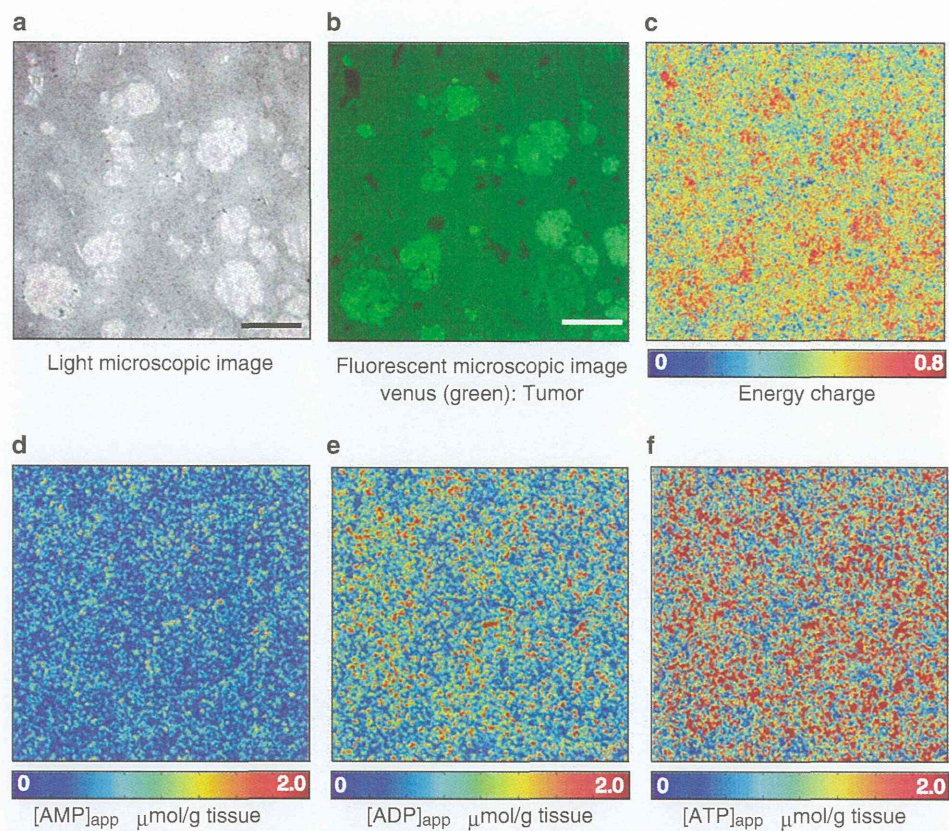


**Fig. 4** Glutathione and UDP-HexNAc as marker metabolites enriched in hepatic cancer metastasis.

**a** Light-microscopic photograph of intrasplenically injected HCT116 colon cancer cell xenografts in the liver of NOG mice. *Scale bar: 500  $\mu$ m.*

**b** A green fluorescence image of the same specimen shown in (a). *Scale bar: 500  $\mu$ m.*

**c** An apparent contents map of UDP-HexNAc at  $m/z$  606.06.

**d, e** Apparent contents maps of the reduced type of glutathione (GSH) at  $m/z$  306.07, and oxidized glutathione (GSSG) at  $m/z$  611.14.

**f**  $[GSH]_{app}/[GSSG]_{app}$  ratio imaging in the same microscopic field plotted as a heat map. A representative set of pictures from four separate experiments

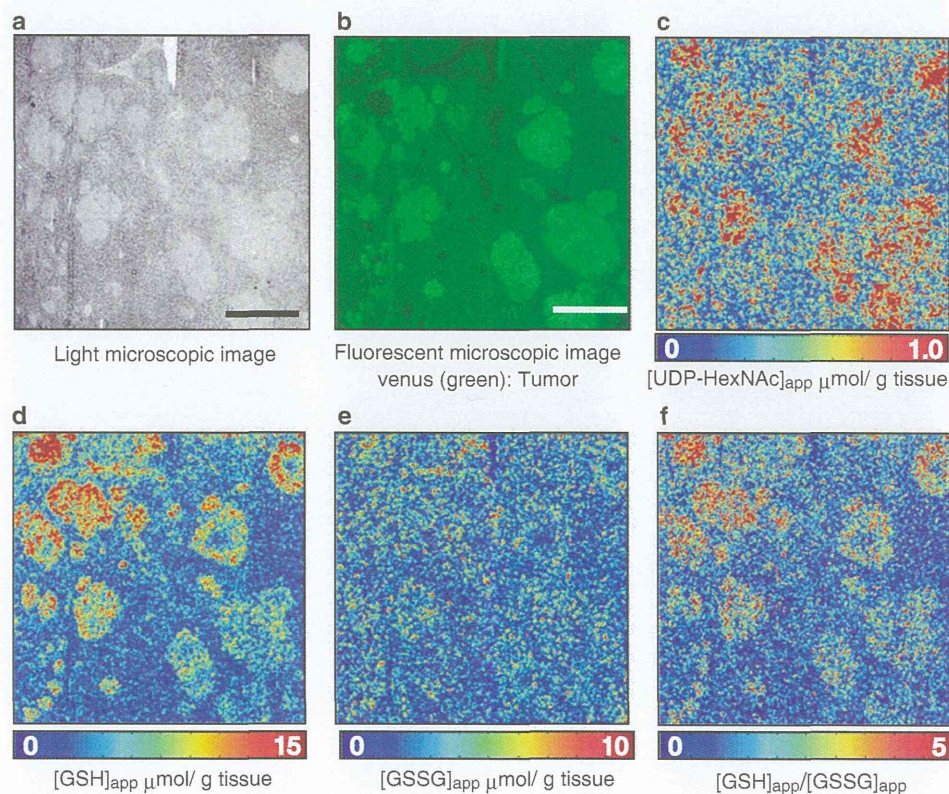
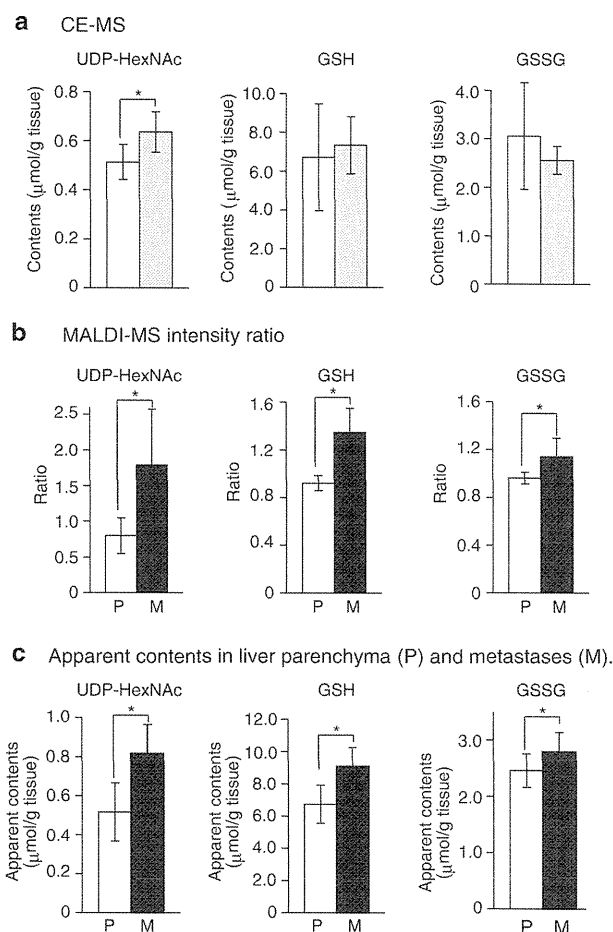


Figure 5 illustrates semiquantitative comparison of these metabolites among different groups. As seen in Fig. 5a showing data collected from CE-MS, amounts of UDP-HexNAc in the tumor-bearing liver (tumor plus liver) were significantly greater than those in the control liver. On the other hand, amounts of GSH and GSSG were not significantly different between the groups. When MALDI-MS intensity ratios in IMS for these metabolites were analyzed (Fig. 5b), UDP-HexNAc, GSH, and GSSG were significantly elevated in the metastatic foci compared with those measured in the hepatic parenchyma. Such a trend was reproducible in the calibrated data showing apparent contents of these metabolites (Fig. 5c), suggesting that both forms of glutathione occurred prominently in the metastatic foci to greater extents than in the host liver parenchyma.

In the control liver, UDP-HexNAc which is an important substrate for polysaccharide chains including hyaluronic acid, was homogeneously distributed over the liver (Fig. 2i). As seen in Fig. 4, on the other hand, the colon cancer xenografts exhibited greater accumulation than the liver parenchyma. Ishimoto et al. and our laboratory have recently provided evidence that CD44, the hyaluronic acid receptor expressed on cancer stem cells, is responsible for stabilization of the cystine transporter xCT that accelerates uptake of cysteine and glutathione to increase their antioxidative capacity against cell death [28]. Because GSH detoxifies electrophiles through their conjugation by glutathione *S*-transferases, such accumulation of the thiol might contribute to survival of the cancer cells against anti-cancer reagents [29, 30]. Up to now, it remains still difficult to visualize amino acids globally by MALDI-MS with high spatial resolution. Improvement of the spatial resolution in the current IMS system together with development of the method to visualize amino acid metabolism deserves further studies provided that resources and mechanisms for delivery of amino acids to maintain GSH in cancer cells are revealed.

## Conclusion

Comparison of differences in metabolomic profiles between control livers and those bearing metastatic foci of the human colon cancer enabled us to reveal distinct metabolic features between the two regions. IMS using 9-aminoacridine enabled us to detect nucleotides, lipids, and several aminosugars. The metastatic human colon cancer xenografts displayed remarkable accumulation of UDP-HexNAc and glutathione *in vivo*, serving as marker metabolites. Newly developed IMS combined with CE-MS measurements serves as a potentially reliable method to perform intergroup comparison of varied metabolites among different tissue specimens. Future investigation is



**Fig. 5** Differences in contents of UDP-HexNAc, and reduced (*GSH*) and oxidized (*GSSG*) glutathione in the tumor-bearing-NOG liver. **a** Differences in CE-MS data between the control (*open columns*) and the tumor-bearing livers (*dark columns*) of NOG mice. **b** The MALDI-MS signal intensity ratio of UDP-HexNAc, GSH, and GSSG in the parenchyma (*P*; *open columns*) and metastatic foci (*M*; *closed columns*) versus the average MALDI-MS intensity of the ROIs as a whole. *Bars* indicate SD. \* $P < 0.05$  according to Mann-Whitney *U*-tests. **c** Apparent amounts of UDP-HexNAc, GSH, and GSSG in the parenchyma (*P*; *open columns*) and metastatic foci (*M*; *closed columns*). *Bars* indicate SD from four separate experiments. \* $P < 0.05$ , Mann-Whitney *U*-tests

necessary to establish methodology for use of the current technique in diagnostic medicine.

**Acknowledgements** The authors are grateful to Masaaki Matsuura (Japan Federation of Cancer Research) and all the member of the SENTAN project (Shimadzu Corporation), Kenji Kawai (Central Institute for Experimental Animals), and members of Suematsu Laboratory for providing considerable support for our research. The authors acknowledge support for this work by a Grant-in-Aid for SENTAN from the Japan Science and Technology Agency (to M.Se. and M.W.) and from the JST ERATO Suematsu Gas Biology Project (to M.Su). Design of CE-MS-based metabolome analysis in this study was supported by Research and Development of the Next-Generation Integrated Simulation of Living Matter, a part of the Development and Use of the Next-Generation Supercomputer Project of MEXT.

**Open Access** This article is distributed under the terms of the Creative Commons Attribution Noncommercial License which permits any noncommercial use, distribution, and reproduction in any medium, provided the original author(s) and source are credited.

## References

- Sugiura Y, Konishi Y, Zaima N, Kajihara S, Nakanishi H, Taguchi R, Setou M (2009) Visualization of the cell-selective distribution of PUFA-containing phosphatidylcholines in mouse brain by imaging mass spectrometry. *J Lipid Res* 50:1776–1788
- Shimma S, Sugiura Y, Hayasaka T, Zaima N, Matsumoto M, Setou M (2008) Mass imaging and identification of biomolecules with MALDI-QIT-TOF-based system. *Anal Chem* 80:878–885
- Khatib-Shahidi S, Andersson M, Herman JL, Gillespie TA, Caprioli RM (2006) Direct molecular analysis of whole-body animal tissue sections by imaging MALDI mass spectrometry. *Anal Chem* 78:6448–6456
- Stoeckli M, Chaurand P, Hallahan DE, Caprioli RM (2001) Imaging mass spectrometry: a new technology for the analysis of protein expression in mammalian tissues. *Nat Med* 7:493–496
- Groseclose MR, Andersson M, Hardesty WM, Caprioli RM (2007) Identification of proteins directly from tissue: in situ tryptic digestions coupled with imaging mass spectrometry. *J Mass Spectrom* 42:254–262
- Edwards JL, Kennedy RT (2005) Metabolomic analysis of eukaryotic tissue and prokaryotes using negative mode MALDI time-of-flight mass spectrometry. *Anal Chem* 77:2201–2209
- Hattori K, Kajimura M, Hishiki T, Nakanishi T, Kubo A, Nagahata Y, Ohmura M, Yachie-Kinoshita A, Matsuura T, Morikawa T et al (2010) Paradoxical ATP elevation in ischemic penumbra revealed by quantitative imaging mass spectrometry. *Antioxid Redox Signal* 13:1157–1167
- Miura D, Fujimura Y, Yamato M, Hyodo F, Utsumi H, Tachibana H, Wariishi H (2010) Ultrahighly sensitive in situ metabolomic imaging for visualizing spatiotemporal metabolic behaviors. *Anal Chem* 82:9789–9796
- Harada T, Yuba-Kubo A, Sugiura Y, Zaima N, Hayasaka T, Goto-Inoue N, Wakui M, Suematsu M, Takeshita K, Ogawa K et al (2009) Visualization of volatile substances in different organelles with an atmospheric-pressure mass microscope. *Anal Chem* 81:9153–9157
- Cooks RG, Ouyang Z, Takats Z, Wiseman JM (2006) Detection Technologies. *Ambient mass spectrometry*. *Science* 311:1566–1570
- Liu Q, Guo Z, He L (2007) Mass spectrometry imaging of small molecules using desorption/ionization on silicon. *Anal Chem* 79:3535–3541
- Nemes P, Barton AA, Vertes A (2009) Three-dimensional imaging of metabolites in tissues under ambient conditions by laser ablation electrospray ionization mass spectrometry. *Anal Chem* 81:6668–6675
- Li Y, Shrestha B, Vertes A (2008) Atmospheric pressure infrared MALDI imaging mass spectrometry for plant metabolomics. *Anal Chem* 80:407–420
- Sroyraya M, Goto-Inoue N, Zaima N, Hayasaka T, Chansela P, Tanasawet S, Shrivastava K, Sobhon P, Setou M (2010) Visualization of biomolecules in the eyestalk of the blue swimming crab, *Portunus pelagicus*, by imaging mass spectrometry using the atmospheric-pressure mass microscope. *Surf Interface Anal* 42:1589–1592
- Takizawa Y, Mizuta K, Hayasaka T, Nakanishi H, Okamura J, Mineta H, Setou M (2010) Specific localization of five phosphatidylcholine species in the cochlea by mass microscopy. *Audiol Neurootol* 16:315–322
- Sun G, Yang K, Zhao Z, Guan S, Han X, Gross RW (2007) Shotgun metabolomics approach for the analysis of negatively charged water-soluble cellular metabolites from mouse heart tissue. *Anal Chem* 79:6629–6640
- Hamada K, Monnai M, Kawai K, Nishime C, Kito C, Miyazaki N, Ohnishi Y, Nakamura M, Suemizu H (2008) Liver metastasis models of colon cancer for evaluation of drug efficacy using NOD/Shi-scid IL2R $\gamma$ <sup>null</sup> (NOG) mice. *Int J Oncol* 32:153–159
- Ito M, Hiramatsu H, Kobayashi K, Suzue K, Kawahata M, Hioki K, Ueyama Y, Koyanagi Y, Sugamura K, Tsuji K et al (2002) NOD/SCID/ $\gamma$ c<sup>null</sup> mouse: an excellent recipient mouse model for engraftment of human cells. *Blood* 100:3175–3182
- Handa K, Ohmura M, Nishime C, Hishiki T, Nagahata Y, Kawai K, Suemizu H, Nakamura M, Wakui M, Kitagawa Y et al (2010) Phosphorescence-assisted microvascular O<sub>2</sub> measurements reveal alterations of oxygen demand in human metastatic colon cancer in the liver of superimmunodeficient NOG mice. *Adv Exp Med Biol* 662:423–429
- Sakuragawa T, Hishiki T, Ueno Y, Ikeda S, Soga T, Yachie-Kinoshita A, Kajimura M, Suematsu M (2010) Hypotaurine is an energy-saving hepatoprotective compound against ischemia-reperfusion injury of the rat liver. *J Clin Biochem Nutr* 46:126–134
- Shintani T, Iwabuchi T, Soga T, Kato Y, Yamamoto T, Takano N, Hishiki T, Ueno Y, Ikeda S, Sakuragawa T et al (2009) Cystathionine  $\beta$ -synthase as a carbon monoxide-sensitive regulator of bile excretion. *Hepatology* 49:141–150
- Soga T, Baran R, Suematsu M, Ueno Y, Ikeda S, Sakuragawa T, Kakazu Y, Ishikawa T, Robert M, Nishioka T et al (2006) Differential metabolomics reveals ophthalmic acid as an oxidative stress biomarker indicating hepatic glutathione consumption. *J Biol Chem* 281:16768–16776
- Kinoshita A, Tsukada K, Soga T, Hishiki T, Ueno Y, Nakayama Y, Tomita M, Suematsu M (2007) Roles of hemoglobin allostery in hypoxia-induced metabolic alterations in erythrocytes: simulation and its verification by metabolome analysis. *J Biol Chem* 282:10731–10741
- Accatino L, Simon FR (1976) Identification and characterization of a bile acid receptor in isolated liver surface membranes. *J Clin Invest* 57:496–508
- Stahl E, Arnesjö B (1972) Taurocholate metabolism in man. *Scand J Gastroenterol* 7:559–566
- Pacifici GM, Rane A (1982) Distribution of UDP-glucuronyltransferase in different human foetal tissues. *Br J Clin Pharmacol* 13:732–735
- Suematsu M, Kato S, Ishii H, Asako H, Yanagisawa T, Suzuki H, Oshio C, Tsuchiya M (1991) Intralobular heterogeneity of carbon tetrachloride-induced oxidative stress in perfused rat liver visualized by digital imaging fluorescence microscopy. *Lab Invest* 64:167–173
- Ishimoto T, Nagano O, Yae T, Tamada M, Motohara T, Oshima H, Oshima M, Ikeda T, Yagi H, Masuko T, et al. (2011) CD44 variant regulates redox status in cancer cells by stabilizing the xCT subunit of system xc- and thereby promotes tumor growth. *Cancer Cell* 19:387–400
- Moscow JA, Fairchild CR, Madden MJ, Ransom DT, Wieand HS, O'Brien EE, Poplack DG, Cossman J, Myers CE, Cowan KH (1989) Expression of anionic glutathione-S-transferase and P-glycoprotein genes in human tissues and tumors. *Cancer Res* 49:1422–1428
- Dang DT, Chen F, Kohli M, Rago C, Cummins JM, Dang LH (2005) Glutathione S-transferase p11 promotes tumorigenicity in HCT116 human colon cancer cells. *Cancer Res* 65:9485–9494

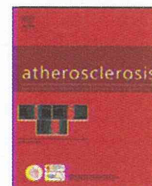




Contents lists available at ScienceDirect

## Atherosclerosis

journal homepage: [www.elsevier.com/locate/atherosclerosis](http://www.elsevier.com/locate/atherosclerosis)



### Imaging mass spectrometry-based histopathologic examination of atherosclerotic lesions

Nobuhiro Zaima<sup>a,b,\*</sup>, Takeshi Sasaki<sup>c,d</sup>, Hiroki Tanaka<sup>a,e</sup>, Xian Wu Cheng<sup>d</sup>, Kenji Onoue<sup>a</sup>, Takahiro Hayasaka<sup>a</sup>, Naoko Goto-Inoue<sup>a</sup>, Hirofumi Enomoto<sup>a</sup>, Naoki Unno<sup>e</sup>, Masafumi Kuzuya<sup>d</sup>, Mitsutoshi Setou<sup>a,\*\*</sup>

<sup>a</sup> Department of Cell Biology and Anatomy, Hamamatsu University School of Medicine, 1-20-1, Handayama, Higashi-ku, Hamamatsu, Shizuoka 431-3192, Japan

<sup>b</sup> Department of Applied Biological Chemistry, Kinki University, 3327-204, Naka-machi, Nara 631-8505, Japan

<sup>c</sup> Department of Anatomy and Neuroscience, Hamamatsu University School of Medicine, Japan

<sup>d</sup> Department of Geriatrics, Nagoya University Graduate School of Medicine, Japan

<sup>e</sup> Department of Vascular Surgery, Hamamatsu University School of Medicine, Japan

#### ARTICLE INFO

##### Article history:

Received 26 November 2010

Received in revised form 18 March 2011

Accepted 30 March 2011

Available online xxx

##### Keywords:

ApoE-deficient mouse

Lipids

Smooth muscle cells

Arachidonic acid

Phosphatidylcholine

Imaging mass spectrometry

#### ABSTRACT

**Aims:** Imaging mass spectrometry (IMS) enables the visualization of individual molecules present on tissue sections. We attempted to identify and visualize specific markers for aortic atherosclerotic lesions. **Methods and results:** Atherosclerotic lesions were obtained from aortic roots of apolipoprotein E (ApoE)-deficient mice at 60 weeks of age and from femoral arteries of humans with peripheral artery occlusive disease. IMS was performed with a matrix-assisted laser desorption/ionization mass spectrometry time-of-flight (TOF)/TOF-type instrument. The molecular ions at  $m/z$  671.6 and 673.6 were found to be specific molecules in the mouse and human lipid-rich regions. These molecules were assigned as cholesterol linoleate (CE 18:2) and cholesterol oleate (CE 18:1). In the case of the human samples, triacylglycerol was also localized in the lipid-rich regions. The distributions of the molecular ions at  $m/z$  804.5 and 832.5 were the same as the distribution of both the mouse and the human SMCs. These molecules were assigned as phosphatidylcholine (PC) (diacyl 16:0/20:4) and PC (diacyl 18:0/20:4). The molecular ion at  $m/z$  566.9 was localized in the mouse calcified regions, and the molecular ions at  $m/z$  539.0 were localized in the human calcified regions.

**Conclusions:** The IMS-based histopathologic examination (IbHE) revealed the characteristic peaks of lipid-rich regions, SMCs, and calcified regions in the atherosclerotic lesions. In addition, IbHE revealed the characteristic distribution of lipids in human atherosclerotic lesions. These data indicate that an IMS-based pathologic approach is of considerable value as a new histopathologic examination.

© 2011 Elsevier Ireland Ltd. All rights reserved.

#### 1. Introduction

Atherosclerosis is a progressive and multigenic vascular disease that involves plaque formation in intimal areas that include various cells and molecules. The development of an atherosclerotic plaque is reported to be closely associated with dyslipidemia and chronic inflammation [1]. The increased permeability of the vascular endothelium causes the intimal accumulation of oxidized low-density lipoprotein (LDL) [2]. Monocytes that are recruited

to the intima and subintima transform into macrophages and foam cells through the increased uptake of modified LDL, thereby leading to the formation of early atherosclerotic lesions (fatty streaks) [1]. Fatty streaks grow into atherosclerotic plaques following the accumulation of inflammatory cells and the evolution of a lipid core region that is surrounded by a cap of smooth muscle cells (SMCs) [3,4]. In the lipid-rich atherosclerotic plaques, such as macrophages or SMCs occurs, and these apoptotic cells form a necrotic core [5]. The persistence of these processes finally leads to vascular calcification and rupture of the plaque [6]. The development of atherosclerosis is accompanied by the progressive alteration of the vascular walls [7]. Therefore, it is important to examine the condition of the vascular walls to estimate the pathology of atherosclerosis. Conventional stainings such as oil staining or immunostaining are essential for examination of the pathologic process of atherosclerosis. However, conventional stainings have 3 weaknesses. The first is that conventional oil staining can-

\* Corresponding author at: Department of Applied Biological Chemistry, Kinki University, 3327-204, Naka-machi, Nara 631-8505, Japan. Tel.: +81 742 43 8067; fax: +81 742 43 8067.

\*\* Corresponding author. Tel.: +81 53 435 2292; fax: +81 53 435 2292.

E-mail addresses: [zaimanobuhiro@gmail.com](mailto:zaimanobuhiro@gmail.com) (N. Zaima), [setou@hama-med.ac.jp](mailto:setou@hama-med.ac.jp) (M. Setou).

not visualize the species of lipids that are strongly involved in the development of atherosclerosis. Although cholesterol is considered the predominant accumulated material in atherosclerotic lesions [8], we recently found characteristic aortic atherosclerotic lesions that accumulate triglycerides (TG) and show normal cholesterol levels [9]. This finding emphasizes the necessity of establishing an examination method that enables the selective visualization of lipids in atherosclerotic lesions. The second weakness is that immunostaining requires several antibodies or sections for the multistaining procedure. The number of sections available is often limited in cases in which local lesions are examined. The third weakness is that immunostaining often cannot detect the low-molecular compounds such as metabolites. Therefore, the simultaneous visualization of biomolecules and component cells in atherosclerotic vascular disease would be useful for the pathologic examination of atherosclerotic lesions.

Imaging mass spectrometry (IMS) is expected to be a suitable tool for investigating the pathologic conditions of atherosclerotic vascular disease. IMS enables the visualization of individual molecules on tissue sections, without requiring antibodies, staining, or complicated pretreatment steps [10,11]. IMS allows the detection of a wide range of biomolecules, such as lipids [12–16], glycolipids [17,18], and proteins [19,20], as well as nutrients [21,22]. In this study, we attempted to identify and visualize specific markers for aortic atherosclerotic lesions using an IMS-based histopathologic examination (IbHE).

## 2. Materials and methods

### 2.1. Chemicals and reagents

2,5-Dihydroxybenzoic acid (DHB) was purchased from Bruker Daltonics (Bremen, Germany). All chemicals used in this study were of the highest purity available.

### 2.2. Ethics

This study was approved by the Ethics Committee of Clinical Research, Hamamatsu University School of Medicine.

### 2.3. Animals

All animal experiments were performed in accordance with the guidelines of Hamamatsu University School of Medicine for Animal Care. Male ApoE-deficient mice with a C57BL/6 genetic background were obtained from the Jackson Laboratory (Bar Harbor, ME). The mice were provided with a standard diet (Oriental Yeast, Tokyo, Japan) and tap water ad libitum.

### 2.4. Tissue collection and processing

The mice (age, 60 or 12 weeks) were euthanized by an intraperitoneal pentobarbital injection, and were perfused through the left cardiac ventricle with isotonic saline and 4% paraformaldehyde in a 0.01 mol/L phosphate buffer, pH 7.4, under physiological pressure. The aortic roots were removed and immersed in fixative (4% paraformaldehyde in a 0.01 mol/L phosphate buffer, pH 7.4) for 16 h (4°C), and then, the samples were embedded in 2% carboxymethyl cellulose (CMC) and frozen in isopentane, which was chilled in liquid nitrogen. Common femoral arteries were harvested from male patients with peripheral artery occlusive disease (PAD) who underwent femoro-popliteal bypass surgery for atherosclerotic samples. After perivascular adipose tissues were carefully removed, femoral arteries were frozen in isopentane without any fixation. Samples were prepared as previously described [23], but with slight modifications. In brief, consecutive 8- $\mu$ m sections were obtained

using a cryostat (CRYOCUT CM 1850; Leica Microsystems, Wetzlar, Germany). The serial sections were mounted onto MAS-coated slides (Matsunami, Osaka, Japan) for histochemical and immunohistochemical staining, and indium-tin oxide (ITO)-coated glass slides (Bruker Daltonics) for imaging mass spectrometry.

### 2.5. Histochemical and immunohistochemical staining

The serial sections were stained with oil red O for the visualization of lipids. The corresponding sections on separate slides were used for the immunohistochemical staining, using rabbit polyclonal antibody against  $\alpha$ -SMC actin (1:50, Thermo Fisher Scientific, CA, USA) for visualization of SMCs. The sections were preincubated with 3% normal goat serum (Vector Laboratories, MI) and then incubated with primary antibodies for 45 min at room temperature. The sections were then reacted with horseradish peroxidase (HRP)-conjugated secondary antibody against rabbit IgG (1:100, Vector Laboratories) for 45 min at room temperature. These sections were visualized with an HRP substrate kit (Vector Laboratories) according to the manufacturer's instructions. The counterstaining for the nucleus was performed with Mayer's hematoxylin.

### 2.6. IMS

50 mg/mL DHB in methanol/water (7/3, v/v) was used as a matrix. A total of 500  $\mu$ L DHB matrix solution was sprayed uniformly over the sections with a 0.2-mm nozzle caliber airbrush (Procon Boy FWA Platinum; Mr. Hobby, Tokyo, Japan). After the slide glass was dried, it was affixed to the mass spectrometer target plate. IMS was performed using a matrix-assisted laser desorption/ionization mass spectrometry (MALDI) time of flight (TOF)/TOF-type instrument (Ultraflex II, Bruker Daltonics) equipped with a 355-nm Nd:YAG laser at a repetition rate of 200 Hz. Data were acquired with a step size of 25  $\mu$ m for mice samples or 50  $\mu$ m for human samples in the positive ion mode (reflector mode). The  $m/z$  values in the range of 400–1000 were measured. The laser diameter was set to the minimum size. The  $m/z$  values were calibrated externally using a peptide calibration standard (Bruker Daltonics). All the spectra were acquired automatically using FlexImaging software (Bruker Daltonics). Normalization of spectra based on total ion current (TIC) was also performed using this software to compare the different samples. The software was also used to create two-dimensional ion-density maps, and peak analyses were performed using FlexAnalysis (Bruker Daltonics). After analysis by IMS, the sections were subjected to hematoxylin–eosin (HE) staining.

### 2.7. Molecular identification

Phosphatidylcholine (PC) and TG were identified by tandem MS (MS/MS) [24]. MS/MS was performed using a MALDI linear quadrupole ion-trap-type instrument (LTQ-XL, Thermo Fisher Scientific) because neutral loss of fatty acids could not be detected by MS/MS using MALDI time of flight (TOF)/TOF-type instrument. The precursor and fragment ions obtained by collision-induced dissociation were ejected from the ion trap and analyzed. The collision energy was set to 30%. The laser energy was set to 30  $\mu$ J. Cholesterol ester (CE) was assigned on the basis of  $m/z$  value.

## 3. Results

Fig. 1a is an HE staining image of an aortic root of ApoE-deficient mouse at 60 weeks of age. We fractionated 3 regions according to the pathologic findings. Region 1 is a lipid-rich region with an insubstantial cell component. This region was positively stained by oil red O staining (Fig. 1b). Region 2 is located in the media and